Journal of Computational Physics **170,** 81–111 (2001)
doi:10.1006/jcph.2001.6723, available online at http://www.idealibrary.com on IDEAL®

Combining Cell- and Point-Centered Methods in 3D, Unstructured-Grid Radiation–Hydrodynamic Codes[1]

A. I. Shestakov, J. L. Milovich, and M. K. Prasad

Lawrence Livermore National Laboratory, Livermore, California 94550
E-mail: shestakov1@llnl.gov; milovich1@llnl.gov; prasad1@llnl.gov

Received March 7, 2000; revised December 27, 2000

We describe the coupling of a cell-centered hydrodynamic scheme to a point-centered finite element method simulating diffusive processes such as heat conduction and radiation transport. We also discuss procedures that compute the material coefficients, the scheme advancing the radiation energy, and how to tally diffusion boundary fluxes in sections with Dirichlet boundary data. To demonstrate the coupling's robustness and accuracy, we simulate the implosion of a radiatively driven inertial confinement fusion capsule. The simulation, done on an unstructured, 3D, tetrahedral grid, maintains spherical symmetry. © 2001 Academic Press

1. INTRODUCTION

The development of codes to simulate inertial confinement fusion (ICF) experiments is difficult because of the variety of equations which must be solved. At a minimum, such codes solve the equations of compressible hydrodynamics, heat conduction, radiation transport, laser energy deposition, and use equation-of-state (EOS) data for multiple real materials. Typically, the codes consist of separate packages coupled by a controlling module. This paper describes the coupling in one such code, ICF3D [1], in which the arbitrary Lagrangian–Eulerian (ALE) hydrodynamics module [2] is based on cell-centered, discontinuous finite elements (FE) while the heat conduction and radiation transport modules use a conventional, point-centered, continuous, and piecewise differentiable FE scheme. It is now widely accepted that cell-centered methods are the best choice to solve the equations

[1] This work was performed under the auspices of the U.S. Department of Energy by the University of California, Lawrence Livermore National Laboratory under Contract W-7405-ENG-48.

0021-9991/01 $35.00

of compressible hydrodynamics while, for diffusion equations, if the mesh is irregular or unstructured, point-centered FE methods are superior. Thus, ICF3D mixes the two centerings in order to avail itself of the best numerical methods for each package.

Since our approach is unconventional—traditionally cell-centered methods are employed for both schemes—we first review the development of diffusion schemes for radiation–hydrodynamic codes in order to motivate our preference for mixing the two approaches. In the following synopsis we focus attention on "fully-implicit" differencing (except coefficients such as the conductivity are evaluated at the previous time level) since such differencing is more robust [3]. There is additional incentive for such temporal discretization. In applications such as radiation transport, the time step Δt, when compared to the other terms, is so large, that each time level effectively solves for the steady-state. Consequently, in these cases, second-order, temporal differencing yields a worse answer.

Our exposition begins with Kershaw [3], who presents a method to discretize a diffusion equation on a two-dimensional, logically orthogonal quadrilateral mesh in cylindrical (R, Z) coordinates. Kershaw's scheme solves for cell-centered unknowns, e.g., the average temperature inside the quadrilaterals. In the same paper, Kershaw lists the following desirable properties of the matrix approximating the diffusion operator:

1. second-order (spatial) accuracy;
2. nonnegative definitiveness $\Rightarrow$ negative eigenvalues and numerical stability;
3. symmetricity $\Rightarrow$ energy conservation;
4. the M-matrix property $\Rightarrow$ positivity of the solution.

Kershaw shows that for general quadrilateral meshes the above conditions cannot always be satisfied and he opts to sacrifice the last one.

Pert [4] extends Kershaw's analysis by examining how properties of the diffusion equation apply to its discretization. He stresses that the matrix approximating the diffusion operator should be nonnegative definite and recalls the fundamental property of diffusion equations, that extrema decay in time. The latter property is shown to be satisfied for the discretized system if the resulting matrix is an M-matrix and differential.

One unfortunate aspect of the Kershaw and Pert (K&P) schemes is a loss of accuracy on sufficiently distorted grids. For example, even if the diffusion coefficient is constant, and only the steady state solution is sought, and the exact solution is a linear function of the coordinates, the K&P schemes do not reproduce it. This implies that if u is a linear function (and the grid is sufficiently distorted), the discretization of $\nabla \cdot \nabla u$ does not vanish. To alleviate such errors, Shestakov, Harte, and Kershaw [5] propose to solve diffusion equations using finite elements. This method brings many benefits (symmetric, differential, conservative, positive definite linear systems, and for triangular or tetrahedral grids, an easy means to guarantee the M-matrix property) but introduces the nontraditional approach of point-centered unknowns.

Because of the difficulty in coupling point-centered diffusion to cell-centered hydrodynamics, cell-centered diffusion schemes continue to be developed. For example, Morel *et al.* [6] propose a cell-centered diffusion scheme (MDHW) for quadrilateral (logically orthogonal) grids which has two advantages over the K&P schemes: (1) If u is linear, the discretization of $\nabla \cdot \nabla u$ does vanish and (2) the solution seems to converge with second-order accuracy, regardless of the smoothness of the mesh. However, MDHW has the following disadvantages: (1) In addition to the cell-centered unknowns, edge-centered unknowns are introduced which *triples* the size of the linear system. (2) In general, the matrix is asymmetric. (3) For severely distorted meshes, the matrix is ill conditioned and although this may be alleviated by a "parallelogram fixup," the fix degrades the accuracy; the discrete Laplacian no longer annihilates linear functions [6]. Moreover, it is not known whether the MDHW discretization of the diffusion operator is negative definite. If not, the resulting linear systems may be ill posed.

To put cell-centered discretizations on a sounder level, Shashkov *et al.*, using the support operators (SO) method, propose a scheme for logically orthogonal quadrilateral grids (Shashkov and Steinberg [7], Hyman *et al.* [8]). The SO scheme of Shashkov and Steinberg (S&S) [7], has theoretical advantages over MDHW since it is based on a careful construction of discrete operators that mimics the analogous properties of the differential operators. As a result, the S&S discretization is symmetric, differential, conservative, and positive definite. There are two variants of S&S which emanate from discretizing a diffusion equation in "flux" form,

$$u - u_0 = -\Delta t \nabla \cdot \mathbf{f}, \quad \mathbf{f} = -D\nabla u, \tag{1}$$

where $\mathbf{f}$ is the flux and u_0 denotes the old time level. The "temperature-based" option substitutes the second equation into the first which yields a second-order equation for u. Unfortunately, if solving on a nonorthogonal mesh, the S&S spatial differencing produces a *dense* matrix. Shashkov and Steinberg claim that this difficulty is overcome since in solving for u, one often resorts to iterative methods which only require computing matrix–vector products. However, we note that as an intermediate step, S&S computes a discrete vector, the analogue of $-D\nabla u$, and this itself requires solving a banded linear system for the vector components. The system couples components in both logical directions and has twice as many unknowns as the scalar, cell-centered temperatures. Hence, this intermediate step is a nontrivial computation.

Shashkov and Steinberg's preferred, "flux-based" method to solve Eq. (1) is to substitute the first equation into the second thereby obtaining a single system for the flux vector components. Unfortunately, this variant makes tacit assumptions about the differentiability of u_0. The method defines $\mathbf{f}$ using a discrete analogue of the gradient, $\mathbf{f} = \mathbf{G}u \doteq -D\nabla u$ and *applies* $\mathbf{G}$ to the first of Eq. (1) producing,

$$\mathbf{f} + \Delta t\mathbf{G}(\nabla \cdot \mathbf{f}) = \mathbf{G}u_0. \tag{2}$$

As a side note, since the "flux-based" method solves for vector components, in 2D, there are twice as many unknowns as cells.

Shashkov and Steinberg present results on a number of test problems [7]. One in particular, the "Random Mesh[2] Example," stands out since it was originally used by MDHW [6] as proof of the lack of convergence of Kershaw's scheme. Table I, which displays results collected from [6] and [7], presents errors using both "relative" L_2 and max norms—see [6] and [7] for definitions. For comparison, Table I includes results obtained with our nodal FE scheme.[3]

In [9], Morel, Roberts, and Shashkov (MRS) present a scheme that addresses the deficiencies of the prior MDHW [6] and S&S [7] schemes, viz., an asymmetric and nonpositive

[2] Figure 8 displays part of the mesh.

[3] The "exact" S&S solution given in [7] is incompatible with the problem formulation. Our simulations use the S&S boundary conditions and we compare with the correct solution.

TABLE I
Errors on Random Mesh Problem[a]

N[b]	K-L_2[c]	M-L_2[d]	S-L_2[e]	F-L_2[f]	M-max[g]	S-max[h]	F-max[i]
10	1.3-2	1.5-2	1.59-2	1.88-3	4.36-2	4.34-2	1.03-2
20	5.1-3	3.8-3	4.06-3	4.31-4	1.04-2	1.05-2	2.48-3
40	8.4-3	9.6-4	1.00-3	1.04-4	3.43-3	3.18-3	1.17-3
80	1.1-2	2.4-4	—	2.81-5	—	—	3.49-4

[a] See [6] and [7] for specification. Error format: K-L_2 entry for $N = 10$ denotes $1.3 \cdot 10^{-2}$.
[b] Denotes the number of mesh points in each coordinate direction.
[c] Relative L_2 norm error for Kershaw scheme (cited in [6]).
[d] Relative L_2 norm error for MDHW scheme [6].
[e] Relative L_2 norm error for S&S scheme [7].
[f] Relative L_2 norm error for our finite element (FE) scheme.
[g] Max norm error for MDHW scheme.
[h] Max norm error for S&S scheme (cited in [7]).
[i] Max norm error for FE scheme.

definitive linear system for MDHW and a dense system in the temperature-based variant for S&S. The MRS proposal combines the support operator and the MDHW methodologies. The resulting matrix is sparse and symmetric positive definite (SPD), allowing usage of robust solvers such as preconditioned conjugate gradients (PCG). However, as in MDHW, both face-centered *and* cell-centered unknowns are introduced, which in 2D makes the system size $\mathcal{O}(3N)$ where N is the number of cells. In addition, one of the original MDHW and S&S selling points is lost—on a skewed mesh, a linear steady solution is no longer reproduced. The MRS scheme seems to be second order and its accuracy is comparable to S&S.

To conclude the discussion of the MDHW and SO schemes [6–9], we note that their extremal properties are unknown. Since nearly all of the published results are for steady state problems, the issue of unphysical transients (negative temperatures) is unresolved. The MDHW and SO schemes increase the number of unknowns; in 2D, the MDHW and MRS schemes by three times while the flux-based SO schemes by two times. If the schemes were extended to 3D meshes consisting of hexahedra, we expect the MDHW and MRS schemes to increase the unknowns proportionally. Additionally, their extension to 3D may not be trivial. Even if restricted to logically cubical grids, for inclusion in Lagrangian codes, such schemes must be extended to cells with nonplanar faces.

Because of such difficulties, we favor finite element methods. Their suitability for diffusion equations is unquestionable. The only reservation may be that they are point centered and their incorporation into traditional cell-centered Lagrangian codes is delicate, but that is one subject of this paper.

In Section 2, we describe the scheme coupling the cell-centered hydrodynamic scheme [2] to point-centered methods used for the diffusion equations. Then, in Section 2.1 we apply it to a test problem coupling hydrodynamics to diffusion. To complete a description of the multiphysics code, Section 3.1 describes how we compute material properties such as the thermal conductivity. Section 3.2 describes the scheme which advances the radiation energy density. (Time advancement of the heat conduction module is similar and easier since only one scalar equation appears.) The code applies conservative methods to equations written in conservation form. During a run, an accounting is made of the existing energy, boundary fluxes, sources, etc. Section 3.3 describes how we tally the boundary flux alongside points with Dirichlet boundary conditions. Section 4 presents results on a problem coupling most of the physics packages. We simulate the implosion of a National Ignition Facility (NIF) capsule driven with a uniform, steady 0.16 keV radiative source. Although the simulation is spherically symmetric, we run it two ways—in 1D and 3D—in order to test the code's ability to maintain sphericity of the converging waves. Concluding remarks are given in Section 5. The code advances the equations using operator splitting. The appendix motivates our choice for the order in which the packages are called.

2. COUPLING PHYSICS MODULES

We denote the densities of mass, momentum, and total matter energy by ρ, $\rho\mathbf{v}$, and ρE. Other variables are the matter pressure p, internal energy e, specific heat $c_{\mathbf{v}}$, radiation energy density E_r, and the Planck and Rosseland averaged opacities κ_P and κ_R.

We now describe how the physics packages are coupled, paying special attention to the reconciliation between changes due to cell-centered and point-centered schemes. The code's time cycle advances the physics packages in the following order:

1. hydrodynamics $(\rho, \rho\mathbf{v}, \rho E, p, e)$,
2. material properties $(T, c_{\mathbf{v}}, \kappa_P, \kappa_R, \ldots)$,
3. laser energy deposition (S_e),
4. heat conduction (T),
5. radiation transport (E_r, T),
6. synchronization (e, E, p).

In the above list, for each package, the parentheses enclose the comma-delimited entities affected. The appendix describes why the packages are advanced in this particular order.

The variables linking the steps are the (matter) internal energy e and the temperature T. The hydrodynamic module is inherently ALE, which implies that matter is advected across cell faces. Step 2 transfers changes in e (due to the hydrodynamics) to T and computes coefficients used in subsequent steps. Step 3 computes S_e, a source of internal energy. Steps 4 and 5 apply point-centered methods to diffusion equations for T and E_r. Lastly, step 6 distributes changes in T to e, E, and p. Hence, at the start of the next time step, the fields are consistent, e.g., the energy (heat) deposited by the laser has been diffused and coupled to E_r, and the cells' pressure is consistent with these changes.

The two fundamental variables e and T have different discrete representations. The former is cell centered and the latter point centered. For the continuum analogues, their changes are proportional to the specific heat,

$$\Delta e = \left.\frac{\partial e}{\partial T}\right|_{\rho} \Delta T = c_{\mathbf{v}} \Delta T,$$

which implies that changes in e from steps 2–5 occur at fixed ρ. Making e and T fundamental (permanent) variables means that they are realigned in steps 2 and 5 by transferring their *changes* rather than computing one variable from the other. We elaborate on this below, but note that this differs from a previous scheme [1] in which after the hydrodynamic step, T was constructed from e.

We now describe the coupling scheme in more detail. First, we note that the code has two hydrodynamic schemes, both cell centered; one is first order, another second order. For the former, for variables such as ρE and p, only cell averages are advanced. In the second-order scheme, ρE and p are allowed to vary in the cell, which in tetrahedral cells is equivalent to giving variables such as ρE a linear representation in terms of the coordinates.[4] In both schemes, e has only a cell-averaged representation, which is computed at the end of step 1 using

$$e = E - \mathbf{v}^2/2. \tag{3}$$

This potentially problematic equation is the weak link of hydrodynamic schemes written in terms of the total matter energy since there is no assurance that Eq. (3) yields $e \geq 0$. Negative energies may arise in test problems such as the one posed by Noh [10] in a region where the fluid is cold and moving, i.e., $E \approx \mathbf{v}^2/2$. In such problems, as a shock passes, if the shock jumps are only slightly in error, the code may compute an erroneous, negative e. Presently, we avoid such cases by always initializing with small and positive temperatures.

In the following, we use subscripts i and c to denote point- and cell-centered variables, respectively, and superscripts to denote values obtained at the end of the various steps. Thus, $T_i^{(0)}$ is the node-centered temperature at the start of the time cycle. Step 2 begins by computing two cell-centered temperatures and a specific heat,

$$T_c^{(0)} = \left(\int_c dV \sum_i \phi_i T_i^{(0)} \right) \Big/ \int_c dV, \tag{4}$$

$$T_c^{(1)} = T\left(\rho_c^{(1)}, p_c^{(1)}, f_c^{(1)}\right), \tag{5}$$

$$\text{and} \quad c_{\mathbf{v}} = \left. \frac{\partial e\left(\rho_c^{(1)}, p_c^{(1)}, f_c^{(1)}\right)}{\partial T} \right|_{\rho}, \tag{6}$$

where we explicitly note the EOS dependence on the mass fractions f which are also advanced by the hydrodynamic scheme. Unless noted otherwise, $c_{\mathbf{v}}$ is cell centered and constant over the cell. Calculation of properties of material mixtures is described in Section 3.1.

Equations (4) and (5) define two temperatures whose difference

$$\Delta T_c^{(2)} = T_c^{(1)} - T_c^{(0)}$$

defines an energy change on the points

$$\Delta \varepsilon_i^{(2)} = \int_\Omega dV\, \phi_i(x) (\rho c_{\mathbf{v}})_c \Delta T_c^{(2)}.$$

The specific heat $c_{\mathbf{v}}$ leads to a point heat capacity

$$C_{\mathbf{v},i} = \int_\Omega dV\, \phi_i(x)\, (\rho c_{\mathbf{v}})_c,$$

which determines the nodal temperature $T_i^{(2)}$, the starting point for steps 3–5,

$$T_i^{(2)} = T_i^{(0)} + \Delta\varepsilon_i^{(2)} / C_{\mathbf{v},i}. \tag{7}$$

Since Eq. (7) may generate unphysical extrema, $T_i^{(2)}$ is min–maxed,[5]

$$T_i^{(2)} = \max\left[T_{\text{floor}}, T_{i,\min}, \min\left(T_{i,\max}, T_i^{(2)}\right)\right],$$

[4] The hydrodynamic variables are discontinuous across the cell faces.

[5] Since only T is min–maxed, energy is conserved.

where $T_{i,\min}$ and $T_{i,\max}$ are formed from $T_i^{(0)}$ and the $T_c^{(1)}$ of the surrounding cells, and T_{floor} is a user-specified lower bound which depends on the problem. After $T_i^{(2)}$ is calculated, step 2 computes other material properties.

Once $T_i^{(2)}$ is known, steps 3–5 are straightforward. Step 3 supplies a (positive) energy source S_e which is diffused by step 4 yielding the intermediate temperature $T_i^{(4)}$. (There is no need for $T_i^{(3)}$.) Step 5 advances $T_i^{(4)}$ by coupling it to the transport equation for E_r which yields the final temperature $T_i^{(5)}$.

The time cycle concludes with step 6 which transfers the nodal temperature change,

$$\Delta T_i^{(6)} = T_i^{(5)} - T_i^{(2)}, \tag{8}$$

to the cells. In order to simplify the discussion, we first describe the procedure used to couple to the first-order hydrodynamic scheme or when running problems in which the hydrodynamic module is not used. The cell-centered analogue of Eq. (8),

$$\Delta T_c^{(6)} = \left(\int_c dV \sum_i \phi_i \Delta T_i^{(6)} \right) \Big/ \int_c dV,$$

defines the final internal and matter energies,

$$\begin{aligned} e_c^{(6)} &= e_c^{(1)} + c_{\mathrm{v}} \Delta T_c^{(6)}, \\ (\rho E)_c^{(6)} &= (\rho E)_c^{(1)} + \rho c_{\mathrm{v}} \Delta T_c^{(6)}. \end{aligned} \tag{9}$$

The energy $e_c^{(6)}$, density ρ, and the EOS define the final pressure,

$$p_c^{(6)} = p\big(\rho_c, e_c^{(6)},\ f_c\big).$$

Equation (9) has no assurance of keeping $e_c^{(6)}$ positive. If this ever happens, the code prints a warning message, resets the energies to floor values, and continues. We have not yet experienced such a failure and do not expect this to happen for the following reasons. First, step 4 diffuses T, hence only points with relatively large T_i decay while those with small values are increased. Thus, only relatively hot cells lose energy. In step 5, T is coupled to E_r, and in Section 3.2 we prove that the coupling scheme limits the decrease of T. Nevertheless, if Eq. (9) yielded $e_c \leq 0$, resetting it to a floor value leads to an anomalous energy gain which is monitored by the energy accounting functions called at the end of the run.

When coupling to the second-order ALE hydrodynamic scheme [2], we note that it advances the total energy moments

$$\int_c dV\, \phi_i(x)(\rho E)(x). \tag{10}$$

Hence, in addition to updating e_c, $(\rho E)_c$, and p_c, we add the energy changes to the moments as follows. For each cell, we first obtain the cell-to-point centered energy densities $(\rho E)_{c,i}^{(1)}$ by noting that

$$(\rho E)^{(1)}(x) = \sum_j \phi_j(x)\, (\rho E)_{c,j}^{(1)}.$$

Multiplying this by a basis function and integrating yields a linear system for the energy density,

$$\int_c dV\,\phi_i(x)\,(\rho E)^{(1)}(x) = \sum_j M_{ij}(\rho E)^{(1)}_{c,j}, \quad M_{i,j} = \int_c dV\,\phi_i(x)\phi_j(x). \tag{11}$$

The solution of these systems is fast since it only involves matrices of order equal to the number of vertices of the cell, e.g., 4 in a tetrahedron. Once $(\rho E)^{(1)}_{c,i}$ is known, the final values are given by

$$(\rho E)^{(6)}_{c,i} = (\rho E)^{(1)}_{c,i} + \rho_c c_{\mathbf{v}}\big(T^{(5)}_i - T^{(2)}_i\big). \tag{12}$$

Multiplying by the mass matrix elements $M_{i,j}$ gives the energy moments.

Once the total energy is known, the cell-to-point centered pressures $p_{c,i}$, are obtained by expanding the equation

$$e(p, \rho, f) = (\rho E)/\rho - v^2/2$$

about the central values which yields an equation for $p_{c,i}$ in terms of p_c, ρ_c, $\rho_{c,i}$, etc. Lastly, if any $p_{c,i}$ or any result of Eqs. (9) or (12) yields anomalously low values, all the point values $(\rho E)_{c,i}$ and $p_{c,i}$ within the cell are reset to the cell-averaged values $(\rho E)_c$ and p_c, respectively, analogous to the Van Leer limiting procedure described in [2].

To summarize, the linchpins are the node-centered and continuous T and the cell-centered e. We couple by mapping changes from one to the other. We conclude this section by presenting results on a problem which stresses the coupling algorithm. The test simulates a point explosion. Gas motion is governed by the hydrodynamic equations supplemented with a diffusive flux of internal energy.

2.1. *Point Explosion with Heat Conduction*

Consider an ideal gas with constant specific heat $c_{\mathbf{v}}$, i.e.,

$$p = (\gamma - 1)\rho e = (\gamma - 1)c_{\mathbf{v}}\,\rho T.$$

Assume that the heat flux

$$H = -\chi_0\,\rho^{\alpha} T^b \nabla T$$

where χ_0, a, and b are constants. The initial density satisfies

$$\rho|_{t=0} = g_0 r^{\kappa},$$

where g_0 and κ are constants. We simulate a point explosion by concentrating the initial energy—all internal—at the center,

$$(\rho E)_{t=0} = (\rho e)_{t=0} = \mathcal{E}_0\delta(r).$$

Outside of the central region the gas is cold, i.e., $p = T = 0$.

Reinicke and Meyer-ter-Vehn (RMV), who analyzed this problem in terms of similarity variables [11], showed that if $\kappa = (1 - 6b)/(2b - 2a + 1)$, then the solution is self-similar and the coupled system of PDEs can be reduced to a system of ODEs. The solution is characterized by a distinct shock and a distinct heat front. Depending on the magnitude of a certain nondimensional parameter, the shock either precedes or follows the heat front. In this section, to validate our point-to-cell coupling scheme, we first present a convergence study of 1D spherical runs and compare our numerical results to integrations of the RMV system of ODEs performed by Bolstad [12]. We then demonstrate that a 3D Cartesian simulation gives similar results. For this problem, given a fixed resolution, the best results, e.g., sharp shocks, are obtained running in pure Lagrangian mode. However, we present results run in ALE mode in order to demonstrate the robustness of the coupling algorithm.

We use the same parameter settings introduced by RMV, i.e.,

$$\gamma = 5/4, \quad c_\mathrm{v} = 1/(\gamma - 1), \quad a = -2, \quad b = 13/2, \quad g_0 = \chi_0 = 1,$$

and concentrate on a "large $\mathcal{E}_0$" case in which the heat front radius $r_h \approx 2r_s$, where r_s is the shock radius. Hence, we set

$$\mathcal{E}_0 = 235.0.$$

Figure 1 displays results obtained from a 1D spherical simulation using 400 (initially uniform) cells to discretize the domain $0 \leq r \leq 1$. The ALE scheme moves the grid points at half the Lagrangian speed. We normalize results to "exact" ODE integrations [12]. (The normalizations in Fig. 1 are slightly erroneous—see Table II for corrections.) The figure shows that the central T and postshock velocity u agree nicely with the exact values while $\max(\rho)$ is approximately 7% low.

Before quantifying the errors, we note that for this problem it is difficult to measure them. Since the variables are discontinuous at either the shock or the heat front, a relative L_1 or

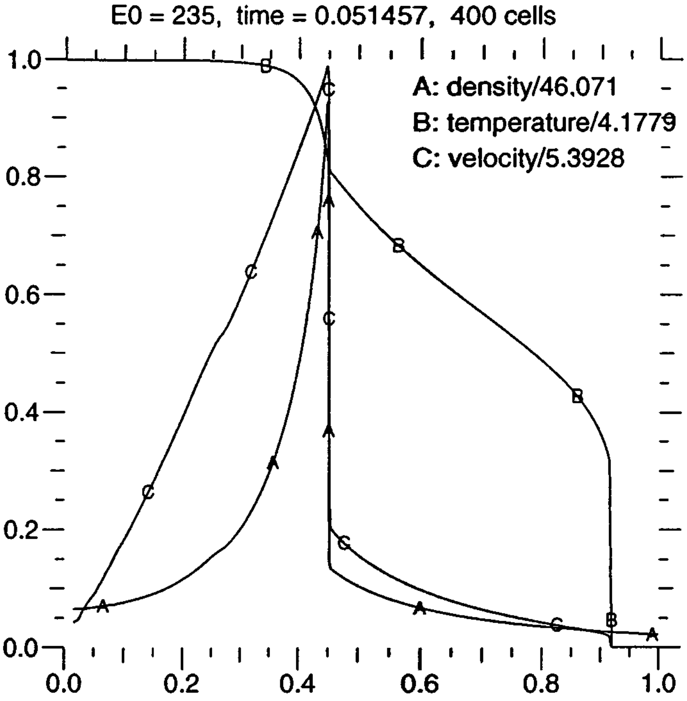

FIG. 1. Self-similar point explosion problem; 1D spherical simulation.

TABLE II
Self-Similar Point Explosion Problem, $\mathcal{E}_0 = 235.0$

N^a	${\rho_{\text{err}}}^b$	${u_{\text{err}}}^b$	${T_{\text{err}}}^c$	${r_s}^d$	${r_h}^e$	$T_{r=0}$
50	22.01	4.88	−1.607	0.417	0.920	4.2417
100	14.91	2.94	−0.345	0.435	0.920	4.1890
200	10.15	1.88	0.002	0.443	0.915	4.1747
400	6.63	1.17	0.053	0.447	0.915	4.1724

[a] Denotes number of cells.
[b] $f_{\text{err}} = 100 \times (1 - f_{\text{code}}/f_{\text{exact}})$; compare at $r = r_s$; $\rho_{\text{exact}} = 45.774$, $u_{\text{exact}} = 5.3925$.
[c] Same as b, except compare at $r = 0$; $T_{\text{exact}} = 4.1746$.
[d] Position of max(ρ).
[e] Largest radius with $T > 1$.

L_2 error measure is inappropriate; numerical fronts are diffused over 1–3 mesh widths and their position varies as $\mathcal{O}(h)$. Furthermore, ρ is especially difficult to approximate near its maximum since it is nearly needle-like at $r = r_s$. Indeed, the ODE integrations show that at $t = 0.05145$, $d\rho/dr \approx 1014$ behind the shock [12]. Thus, even if we only compare maxima, we expect fairly large errors for max(ρ). On the other hand, in regions where the solution is well behaved, e.g., $T(r = 0)$, the errors should be considerably smaller.

There are additional difficulties. First, although we specify a stop time $t_s = 0.05145$, the simulations continue until the first cycle for which the running time exceeds t_s. Thus, simulations with different mesh sizes do not halt at the same time. Secondly, it is difficult to ensure that our simulations (in which $\mathcal{E}_0 = 235$) match RMV's or Bolstad's since there is no explicit relationship between the RMV nondimensional parameter β_0 and $\mathcal{E}_0$—see [11] and [13]. Thirdly, we will examine convergence of max(ρ, u, T) and the positions r_s and r_h. For the analytical solution, the shock location r_s coincides with the location of max(ρ, u), and the heat front r_h is at the outermost radius where $T > 0$. However, since numerical fronts are diffused, defining their position is subjective. In the following, we define r_s as the location of max(ρ) and r_h as the outermost radius where $T > 1$. (The "cold" region is initialized with a positive but small T.) Furthermore, the locations of max(ρ) and max(u) either colocate or are in adjoining cells. The main point is to have consistent definitions and realize that r_s and r_h may lag behind the correct values by 1–2 cell widths.

Results are summarized in Table II in which we display relative % errors in max(ρ, u, T) and positions of the shock r_s and heat r_h fronts. As expected, T has the smallest errors. The values in the last column display second-order convergence, albeit to 4.171 instead of to 4.1746, the result from the ODE integrations. In any case, 200 cells are sufficient to obtain an accuracy better than 0.1% for T. For ρ and u, the errors are larger, but as stated above, these variables are sharply peaked and furthermore, since the numerical values are only cell averages, they are necessarily smaller. The fronts r_s and heat r_h also converge. By any measure, our simulations not only converge, they agree nicely with the ODE integrations.

We next demonstrate the code's performance on a 3D simulation of the same problem. We discretize the unit cube $(0 \leq X, Y, Z \leq 1)$ into 104 initially uniform cells per dimension (over 1.1 million cells).[6] The point explosion is simulated by loading 235/8 units of energy into the corner cell next to the origin. All other cells are initialized with a small pressure.

[6] We use 104 since it is divisible by 8, thereby allowing us to run in parallel on 128 processors by subdividing the domain into blocks of size $13 \times 26 \times 26$.

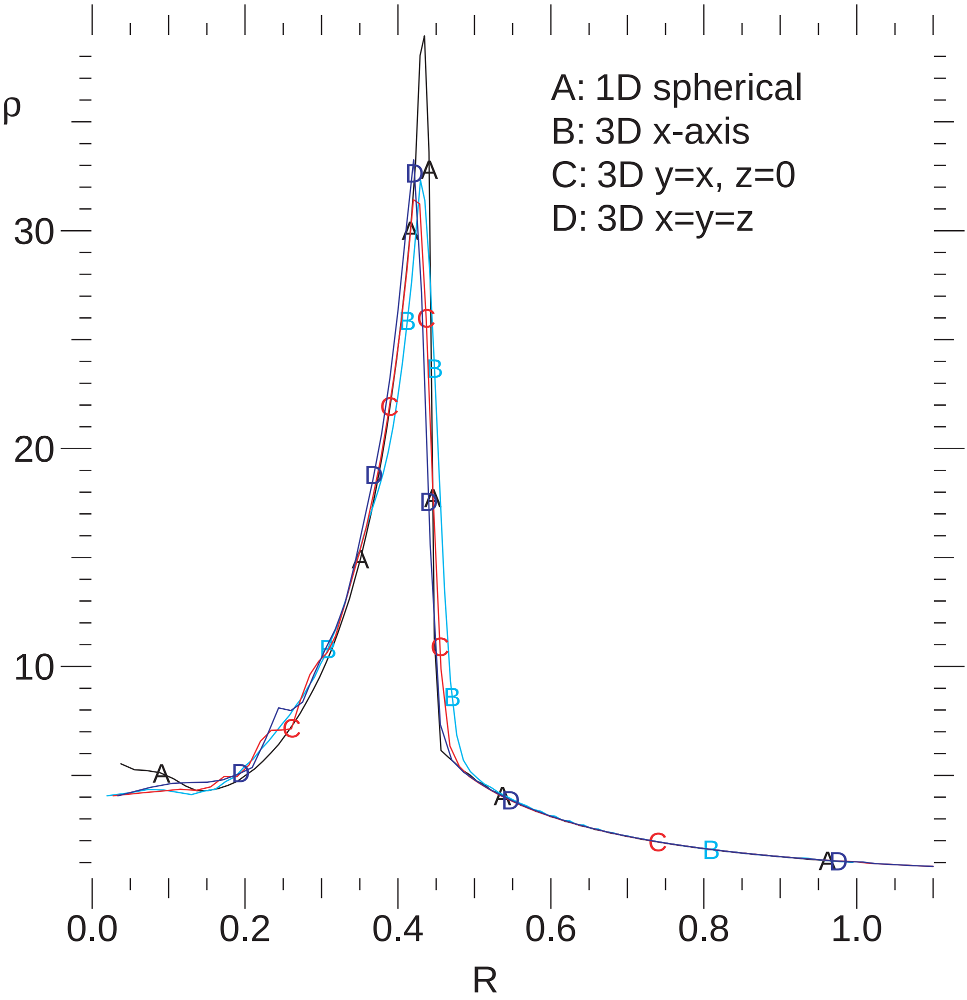

FIG. 2. Self-similar point explosion problem. Density vs. spherical radius. Curve A is a 1D, 100-cell spherical result. Curves B–D are lineouts of the 3D, 104^3-cell Cartesian simulation.

We use Gaussian quadrature to compute the proper cell-averaged initial density. Symmetry is imposed at the $X = 0$, $Y = 0$, and $Z = 0$ planes. The simulation is done in ALE mode; grid points move at 3/10 of the Lagrangian speed.

Our 3D results are summarized in Figs. 2 and 3 in which we display lineouts of ρ and T at the final time $t = 0.05146$. For comparison, the figures also contain results from a 1D, spherical coordinate run using 100 cells. The 3D lineouts are taken along three different directions in order to show near-sphericity of the waves. Figure 2, which displays ρ, shows that although the 3D Cartesian run does not attain the same spherical maxima, the shock locations are nearly coincident. Figure 3, which displays T, is less satisfactory. The 3D central values are somewhat higher than the 1D run and the heat front propagates slightly further along the line $Z = 0$, $Y = X$ and the line $X = Y = Z$, i.e., diagonally across the mesh. However, along the X-axis, T is nearly identical to the 1D run; both fronts are at $r \approx 0.92$. At first blush, since $T \propto e$ and ρe is the internal energy density, and since the

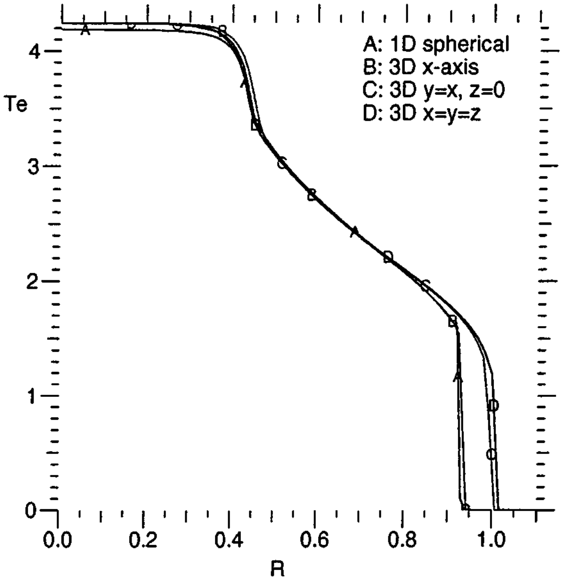

FIG. 3. Self-similar point explosion problem. Temperature vs. spherical radius. Curve A is a 1D, 100-cell spherical result. Curves B–D are lineouts of the 3D, 104^3-cell Cartesian simulation.

3D temperature is generally larger than the 1D result, one might opine nonconservation of energy. This is false, since the code conserves total energy. In fact, at the end of the run, we observe that energy is conserved to 10 decimal places! It then appears that a good measure of error would be to compute the ratio of the internal to total energy. Unfortunately, at the time of this writing, we do not know the “analytic” value. For the record, in our 3D run, at $t = 0.05146$,

$$\left(\int \rho e \, dV\right) \Big/ \left(\int \rho E \, dV\right) = 0.7436.$$

To summarize, considering the extreme nonlinearity of the problem, our simulations generally agree with the independent ODE integrations.

3. PHYSICS PACKAGES

Some of the algorithms for the packages listed in Section 2 have been presented previously. Reference [2] describes the hydrodynamic scheme. The heat conduction module and the laser package are discussed in [1] and [14], respectively. Control of a run, i.e., initialization and what makes its execution transparent for uniprocessors as well as massively parallel systems is delineated in [15]. A discussion of the parallelization of the modules is found in [16] while a parallelization scaling study appears in [17]. In this section, we describe the packages that have not been discussed elsewhere. We first consider the calculation of material properties. Then we describe and analyze the frequency-averaged radiation diffusion package. As a run progresses, the code tallies the conserved quantities: mass, momentum, and energy. Section 3.3 describes the tally for diffusion equations with Dirichlet boundary conditions.

3.1. *Material Coefficients*

We now describe how to compute the material coefficients needed by the other physics packages. The starting point is the equation of state (EOS) for mixed materials which, when given values of two thermodynamic variables, returns the other two, typically $e(\rho, T)$ and $p(\rho, T)$. Recalling the steps described in Section 2, after the hydrodynamic step, for each cell we compute $T_c^{(1)}$ using Eq. (5), other material properties such as $c_{\mathbf{v}}$ using Eq. (6), and the Planck and Rosseland mean opacities κ_P and κ_R.

Our EOS module allows mixtures. The third argument f in Eqs. (5) and (6) is a vector of mass fractions whose individual components $f_i = m_i/m$, where m_i and m are respectively the mass of material i and the total mass in the cell. If a cell is composed of only one material, the EOS call (done cell by cell) branches to the appropriate table for that material. If the cell contains a mixture, we assume that the sum of the individual volumes equals the cell volume, i.e., $\sum_i V_i = V$. If this equation is divided by the masses we obtain

$$\sum_i f_i/\rho_i = 1/\rho,$$

where ρ_i is the individual material density. We also require that all the materials within a cell be at a common pressure and temperature $T_c^{(1)}$. This assumption, while not hydrodynamically correct, is justified by step 4. (In ICF the high thermal diffusion coefficients homogenize the temperature discrepancies within a cell.) Once the ρ_i are computed, average material properties such as e, $c_{\mathbf{v}}$, κ_P, and κ_R are given by equations of the type

$$\bar{g} = \sum_i f_i g_i, \tag{13}$$

where $g_i = e_i, c_{\mathbf{v},i}, \kappa_{P,i}$, or $\kappa_{R,i}$.[7]

For the laser deposition and heat conduction packages, we need the average charge state Z^*, the free electron density n_e, and the Coulomb logarithm $\ln \Lambda$. These quantities are computed using the Thomas–Fermi average atom model [18] in which the material within the cell is said to consist of atoms whose averages are also obtained by Eq. (13) where now $g_i = 1/A_i, Z_i/A_i, Z_i^2/A_i$ and $Z_i \ln Z_i/A_i$ define the average atomic number $\bar{A}$, charge $\bar{Z}$, etc.

We compute Z^*, $\ln \Lambda$, and the thermal (diffusion) coefficient D_e using formulae from More [21] with modifications suggested by Zimmerman [22]. The average charge Z^* and $\bar{A}$ are used to compute the ion and free electron densities

$$n_i = \rho\,\mathcal{A}/[\bar{A}(1 + Z^* m_{ei})] \text{ and } n_e = Z^* n_i,$$

where $\mathcal{A}$ is Avogadro's number and m_{ei} is the ratio of the electron and proton masses.

To conclude this section, we present plots of Z^* and the thermal conductivity D_e, and just like Lee and More [23] (Fig. 4, p. 1278) we examine aluminum. Figure 4 displays $D_e/T^{5/2}$ as a function of T for various ρ. (We plot the ratio $D_e/T^{5/2}$ in order to remove the analytic dependence on the temperature power.) In Fig. 5, we display Z^* for the same density and temperature range.

[7] In the absence of spectral information about the individual opacities, Eq. (13) is also used to compute κ_R.

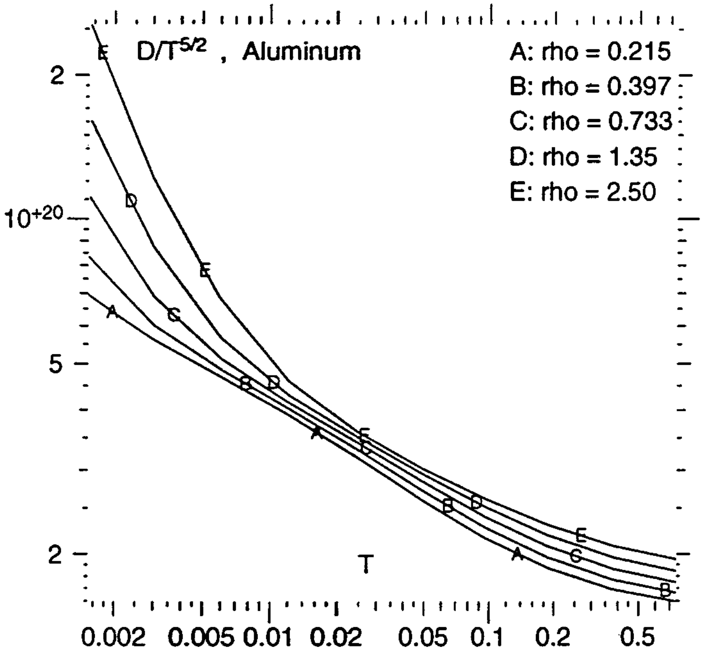

FIG. 4. Aluminum $D_e/T^{5/2}$ vs. T for various ρ. Units: D_e in erg/(cm s keV), T in keV.

In order to avoid superthermal electrons, we limit D_e so that the flux $|D_e \nabla T|$ does not exceed

$$\mathcal{F}_{e,\max} = n_e kT \sqrt{8kT/(\pi m_e)},$$

where m_e is the electron mass.

3.2. *Radiation Transport*

Ignoring effects such as the convection of radiation, radiation pressure, Compton scattering, etc., the relevant equations are

$$\begin{aligned} \partial_t E_r &= \nabla \cdot D_r \nabla E_r + c\rho\kappa_P[B(T) - E_r] \\ \rho c_v \partial_t T &= -c\rho\kappa_P[B(T) - E_r]. \end{aligned} \tag{14}$$

In Eqs. (14), E_r is the energy density of the radiation field; D_r is defined using the Rosseland mean free path,

$$D_r = c\ell_R/3; \tag{15}$$

κ_P is the Planck averaged opacity; and the frequency averaged source function

$$B(T) \doteq (4\sigma/c)T^4 = \int_0^\infty d\nu\, B_\nu(T),$$

where $\sigma = 2\pi^5 k^4/15h^3c^2$ is the Stefan–Boltzmann constant, and $B_\nu(T)$ is the Planck function.

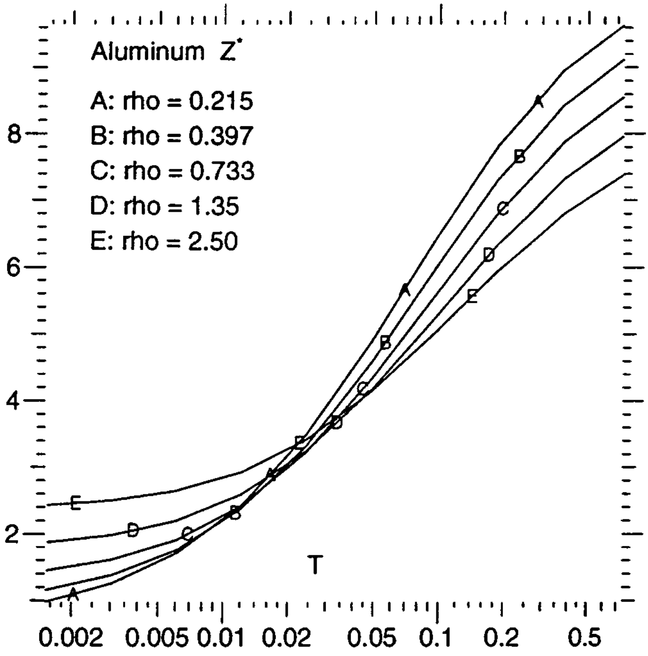

FIG. 5. Average charge Z^* vs. $\log(T)$ with T in keV for various ρ.

Equations (14) are solved using a simplification of the partial temperature scheme described in [5]. If E_r^0 and T^0 denote the variables to be time advanced,[8] we first linearize B,

$$B(T) = B^0 + B^{0'}(T - T^0), \tag{16}$$

where

$$B^0 = B(T^0) \quad \text{and} \quad B^{0'} = (dB/dT)|_{T=T^0}.$$

Using backward Euler temporal differencing, giving E_r, T, and B a point centered, FE representation; then multiplying the second of Eqs. (14) by a test function ϕ_i, integrating; and lumping the integrals, the temperature change at the points is

$$T_i - T_i^0 = \mathcal{K}_i\left(E_{r,i} - B_i^0\right)/\left(\mathcal{C}_i + \mathcal{K}_i B_i^{0'}\right), \tag{17}$$

where

$$\mathcal{C}_i = \int_\Omega dV\, \phi_i(\rho c_{\mathbf{v}})_c \quad \text{and} \quad \mathcal{K}_i = c\Delta t \int_\Omega dV\, \phi_i(\rho\kappa_P)_c, \tag{18}$$

where the subscript c denotes variables which are constant over the cell (zone) and where the subscript i denotes the value at the $\mathbf{x}_i$ vertex.

[8] According to the definitions of Section 2, T^0 is $T_i^{(4)}$, the point-centered temperature after heat conduction.

If Eq. (17) is substituted into Eq. (16) and the result substituted into the first of Eqs. (14), we obtain the scalar equation for $E_{r,i}$,

$$V_i\left(E_{r,i} - E^0_{r,i}\right) = -\sum_j \mathcal{D}_{ij} E_{r,j} + \mathcal{L}_i\left(B^0_i - E_{r,i}\right), \tag{19}$$

where

$$\mathcal{D}_{ij} = \Delta T \int_\Omega dV\, \nabla\phi_i \cdot D_r \nabla\phi_j, \quad V_i = \int_\Omega dV \phi_i, \quad \text{and} \quad \mathcal{L}_i = \mathcal{C}_i \mathcal{K}_i \big/ \left(\mathcal{C}_i + \mathcal{K}_i B^{0'}_i\right). \tag{20}$$

Equation (19) is a FE discretization of a diffusion equation with an explicit source B^0 and a coupling coefficient $\mathcal{L}_i$. To summarize, the scheme consists of computing $\mathcal{L}_i$, solving Eq. (19) for E_r, and computing T_i using Eq. (17).

To prove stability, note that since $\mathcal{L}_i$ and B^0_i are positive, it follows that if the grid is sufficiently fine, Eq. (19) leads to a linear system with an M-matrix. Hence, if $E^0_{r,i} \geq 0$, then $E_{r,i} \geq 0$. Using the definitions for B^0_i and $B^{0'}_i$, Eq. (17) may be used to show that if $E_{r,i} \geq 0$ and $T^0_i \geq 0$, then $T_i \geq 0$. Thus, the scheme yields nonnegative E_r and T. To derive an upper bound for T_i, note that Eq. (17) may be manipulated to yield

$$T_i \leq T^0_i + E_{r,i}\mathcal{K}_i \big/ \left(\mathcal{C}_i + \mathcal{K}_i B^{0'}_i\right). \tag{21}$$

Thus, T_i is bounded by a linear combination of T^0_i and $E_{r,i}$. The latter is itself bounded by $\max_i(E_{r,i})$ which may be estimated using the maximum principle for elliptic equations.

We now analyze the scheme for the two limits, large Δt and large $\mathcal{K}_i$. In the former, the left side of Eq. (19) vanishes and $E_{r,i}$ satisfies a nonhomogeneous Poisson equation which imposes the usual bounds on E, and the manipulations leading to Eq. (21) yield

$$\lim_{\Delta t \to \infty} T_i = \left(3B^0_i + E_{r,i}\right) \big/ B^{0'}_i. \tag{22}$$

For the analysis of large $\mathcal{K}_i$, if the diffusive term in Eqs. (14) is ignored, the scheme reduces to backward Euler differencing of two coupled ODEs, a method known to be stable. In terms of the matter and radiation energies, the result is

$$\lim_{\kappa \to \infty} E_{r,i} = \alpha E^0_{r,i} + (1-\alpha) B^0_i,$$
$$\lim_{\kappa \to \infty} \mathcal{C}_i T_i = \beta \mathcal{C}_i T^0_i + (1-\alpha) V_i E^0_{r,i},$$

where $0 < \alpha = V_i/(V_i + \mathcal{L}_i) < 1$, and $0 < \beta < 1$. It is also easy to show that the scheme is conservative, i.e., whatever energy leaves one field goes to the other.

Our scheme has the drawback that in the limit of large Δt, $E \neq B(T)$ and the solution depends on the previous state. To see this, note that as $\Delta t \to \infty$, Eq. (19) shows that E_r depends on the old source B^0. Also, from Eq. (22) we obtain $E \approx [4(T/T^0) - 3]B^0$. (It is trivial to show that $T/T^0 \geq 3/4$ which also shows the maximum drop that T may incur.) Ensuring $E \approx B(T)$ for large Δt could be addressed by introducing nonlinear Newton iterations at each time step, but this would need to be the subject of another paper.

The fact that when Δt is large the new state depends on the old leads to erroneous answers in some problems. Specifically, the new temperature T_i can be unphysically large.

If Δt is large, the worst error arises if the denominator of Eq. (17) is replaced by $\mathcal{K}_i B_i^{0'}$, which is valid whenever

$$\mathcal{C}_i \ll \mathcal{K}_i B_i^{0'}. \tag{23}$$

To analyze Eq. (23), we note that if e is the matter specific energy, then $c_{\mathbf{v}} \approx e/T$ and $B' \approx B/T$. Hence, Eq. (23) implies

$$\rho e^0/T^0 \ll c\Delta t \rho\kappa_P a (T^0)^4/T^0, \tag{24}$$

where the radiation constant $a = 1.37 \cdot 10^{14}$ erg/cc keV^4. For a monatomic gas, $e = c_{\mathbf{v}} T$, where $c_{\mathbf{v}} \approx 10^{15}$ erg/g keV. Thus, Eq. (23) implies

$$1.82\rho/(T^0)^3 \ll (c\Delta t)(\rho\kappa_P). \tag{25}$$

This condition is obviously problem dependent. The right side is the ratio of the distance radiation travels during the time cycle $(c\Delta t)$ to the mean free path $1/(\rho\kappa_P)$. This ratio may indeed be large, especially if we recall that approximating radiation transport by diffusion is valid only for short mean free paths. In any case, assuming Eq. (23) holds, Eq. (17) has the form

$$T_i = T_i^0 + \left(E_{r,i} - B_i^0\right)/B_i^{0'}.$$

It follows that if T_i^0 is negligibly small, Eq. (22) becomes

$$\lim_{\Delta t\to\infty} T_i = E_{r,i}/4a\left(T_i^0\right)^3, \quad \text{as } T_i^0 \to 0.$$

This is unphysical if the problem involves radiation flow into cold matter since for small enough T^0, the new emission term aT^4 may be greater than E. Hence, at that point, the matter is cooled rather than heated. However, we stress that the limit $T^0 \to 0$ is incompatible with Eq. (25). Hence, the above error should rarely occur for real problems. Nevertheless, it can arise for problems such as the one described in Section 3.2.1 in which $c_{\mathbf{v}}$ also has a T^3 dependence. In that case, the left side of Eq. (25) depends only on ρ.

Before concluding this section, we note that since diffusion is characterized by infinite propagation speeds, a flux-limiter is required. To this end, the coefficient D_r is modified so as to keep the speed of propagation of the radiation energy flux comparable to c. Our modification replaces ℓ_R (see Eq. (15)) with

$$\ell_R' = \ell_R/[1 + (2\ell_R/3)(|\nabla E_r|/|E_r|)]. \tag{26}$$

Equation (26) refers to cell-centered variables, i.e.,

$$|\nabla E_r|_c^2 = \left(\int_c dV |\nabla E_r|^2\right)\Big/\int_c dV,$$

where the gradient is computed using the finite element representation of E_r in the cell,

$$E_r(x) = \sum_i \phi_i(x) E_{r,i},$$

and the cell average $|E_r| = E_{r,c}$ is obtained by applying Eq. (4) to E_r. The flux-limiter is effective in regions of large ℓ_R and in such cases the flux becomes

$$\lim_{\ell_R \to \infty} -D_r \nabla E_r = -(c/2)\left(\left|E_r^0\right| / \left|\nabla E_r^0\right|\right) \nabla E_r,$$

where the superscript denotes a temporally explicit correction. In the limit of small Δt the flux reduces to $cE_r/2$.

In the following sections, we consider two problems which test the radiation module. The first stresses the coupling between E_r and T; the second tests the flux-limiter.

3.2.1. Pomraning problem. We consider a problem proposed by Pomraning [24], in which an initially cold half space of material $(0 \leq Z)$ is irradiated on one side. For this problem, in Eqs. (14) and (15), we fix

$$\rho = \kappa = \ell_R = 1$$

and let $c_{\mathbf{v}}$ have the dependence

$$c_{\mathbf{v}} = c_{\mathbf{v},0} T^3, \quad c_{\mathbf{v},0} = \text{const.} \tag{27}$$

This problem is a stringent test of the scheme since we linearize both B and the matter energy change by writing $\Delta e = c_{\mathbf{v}}(T^0)\Delta T$.

The problem has two parameters, ϵ and F_{inc}. The first is defined by the ratio

$$\epsilon = 16\sigma / c\, c_{\mathbf{v},0}.$$

In the simulation, we use

$$\epsilon = 0.1.$$

The second parameter F_{inc} is used in the boundary condition imposed at $Z = 0$,

$$(c/2)E_r - D_r \partial_Z E_r = 2F_{\text{inc}}. \tag{28}$$

If we define $E_{\text{inc}} = 4F_{\text{inc}}/c$ and set $E_{\text{inc}} = 1$, then Eq. (28) is of the form described in Eq. (32) where $a = b = c/2$.

We present results in Fig. 6 in which we plot E_r and $B(T)$ as functions of Z for various values of the normalized time

$$\tau = \epsilon c \kappa_P t.$$

The results show how the terms E_r and $B(T)$ equilibrate. At $\tau = 0.001$, the two fields differ significantly; at $Z = 0.01$, $E_r > 1000B$. However, by $\tau = 10.0$, $E_r \approx B(T)$. These results are in agreement with those published by Su and Olson [25] (p. 350, Fig. 3).

The simulation uses 100 cells with equal ratio grid spacing. The first cell (at $Z = 0$) is of width $\Delta = 0.01$ and the successive widths increase by 5%. Thus, the computational domain is $0 \leq Z \leq 26.10$ and for the last cell $\Delta = 1.252$. The simulation takes 334 time cycles to reach $\tau = 10.38$. As the run progresses, $\Delta\tau$ increases. Initially, $\Delta\tau = 3.0 \cdot 10^{-11}$; at the end, $\Delta\tau = 0.657$. The code increases the time step by 10% if the fields, when they are above certain base values, do not change appreciably. In this problem, we use $E_{r,\text{base}} = B(T)_{r,\text{base}} = 10^{-5}$.

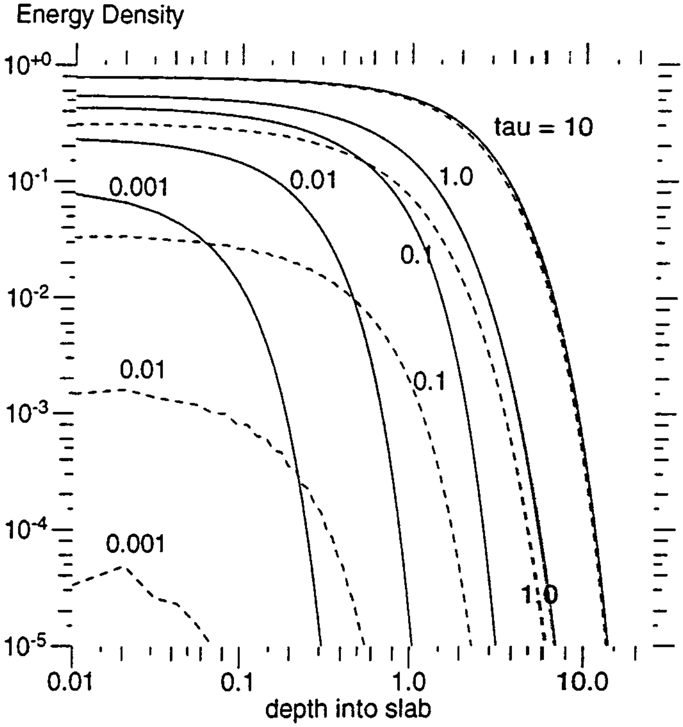

FIG. 6. Pomraning promblem; E_r (solid lines) and $B(T)$ (dashed lines) vs. Z for various τ.

To further demonstrate the accuracy of the scheme, in Table III we display the percentage of relative errors from our results compared to the tabulated values of [25] (p. 346, Tables 1 and 2). Table III shows that our result compares very well except where $B(T)$ has relatively low energy.

In order to demonstrate that the scheme does not introduce any anomalous diffusion as we mix cell- and node-centered methods, in Table IV we compare our $B(T)$ values to those of [25] (p. 346, Table 2) at the leading edge of the front which we define as the position where $B(T)$ exceeds 10^{-4}. In Table IV, we evaluate $B(T)$ by interpolating the result at the mesh points enclosing the desired value of the coordinate $x = \sqrt{3}\kappa Z$ used in [25]. The

TABLE III

Pomraning Problem[a]

τ	$e_{r,0}$	$e_{m,0}$	$e_{r,1}$	$e_{m,1}$
0.001	0.13	—	—	—
0.01	0.21	23.43	20.0	—
0.1	0.20	6.98	0.64	21.18
1.0	0.12	1.10	0.20	0.28
10.0	0.16	0.16	0.40	0.42

[a] Percentage errors $100 \times (f/f_e - 1)$ where f and f_e are our computed results and the exact results (from [25]), respectively. $e_{r,x}$ and $e_{m,x}$ are the errors in the radiation and matter energies at position $x = \sqrt{3}\kappa Z$. Thus, for $\tau = 0.001$, at $Z = 0$, our E_r differs by only 0.13% from the tabulated results of Su and Olson. Because of the accuracy cited in [25], comparison is made only at positions where the function value exceeds 10^{-4}.

TABLE IV
Pomraning Problem[a]

τ	x	B_{su}	B
0.01	0.5	1.2	1.6
0.1	2.5	3.5	3.9
1.0	7.5	2.8	3.0
10.0	15.0	9.8	12.1

[a] Comparion of $B(T)$ at position $x = \sqrt{3}\kappa Z$, at the leading edge of the wave (see text). B_{Su} and B are values of exact (from [25]) and computed results multiplied by 10^4, respectively.

Table II results belie the accuracy attained, since upon closer examination we note that our value where $B \approx 10^{-4}$ is within a mesh width of the position given in [25]. We also note that the results in [25] are guaranteed to be correct to an accuracy of only 10^{-4}.

Before ending this section, we return to the discussion in Section 3.2 regarding the possibility of obtaining anomalously high temperatures when radiation propagates into cold material if Δt is large. Since here $c_{\mathbf{v}} \propto T^3$, Eq. (24) reduces to $c_{\mathbf{v},0} \ll c\Delta t\kappa_P$, and it is easily checked that the parameters for this problem satisfy the inequality. To illustrate the difficulty, if t is normalized by τ, for the Pomraning problem Eqs. (14) become

$$\begin{aligned} \partial_r E &= \nabla \cdot D\nabla E + (1/\epsilon)[B(T) - E] \\ \partial_r e &= -(1/\epsilon)[B(T) - E], \end{aligned} \tag{29}$$

where $D = 1/(3\epsilon)$, $e = B/\epsilon$, and $B = aT^4$. In deriving Eqs. (29), we used $\kappa_P = \rho = 1$. Hence, $e = \rho e$ is now the internal energy density. The normalized time $\tau = \epsilon c\kappa_P t$.

In the Pomraning problem, which simulates radiation propagating into cold material, $B \leq E$. Since Eqs. (29) imply that ϵ is an approximate time for the fields to equilibrate, it is interesting to examine what happens at very early times using the backward Euler, semiimplicit scheme described in Section 3.2. Table V displays the exchange term $-(B_i - E_i)$ at the first few mesh points. A nonuniform mesh is used; $\Delta z_0 = 0.01$, and for $i > 0$, $\Delta z_i = \Delta z_0\,(1.05)^i$. The table shows that for $\Delta\tau_0 = 10^{-8}$, at the incident edge, $B_0 > E_0$, violating physical expectations. For larger $\Delta\tau_0$ the result is worse, e.g., if $\Delta\tau_0 = 10^{-6}$, then after one cycle $-(B_0 - E_0) = -1.2 \cdot 10^{15}$. However, we note that the difficulty arises only if the *initial* time step is too large. The results in this section use $\Delta\tau_0 \approx 10^{-10}$, but $\Delta\tau$ is allowed to increase over the course of the run. Eventually, $\Delta\tau$ grows by over 10 orders of magnitude.

TABLE V
Pomraning Problem[a]

$\Delta\tau_0$	τ	$i = 0$	$i = 1$	$i = 2$	$i = 3$	$i = 4$
1.e-8	1.e-8	−1.5e-1	3.2e-8	9.6e-13	2.6e-16	6.2e-20
1.e-9	1.14e-8	1.1e-5	2.4e-9	3.4e-13	3.6e-17	3.1e21
1.e-10	1.09e-8	1.1e-5	2.0e-9	2.4e-13	2.1e-17	1.4e-21

[a] Energy exchange term $(E_i - B_i)$. First and second columns denote initial time step and current time, respectively.

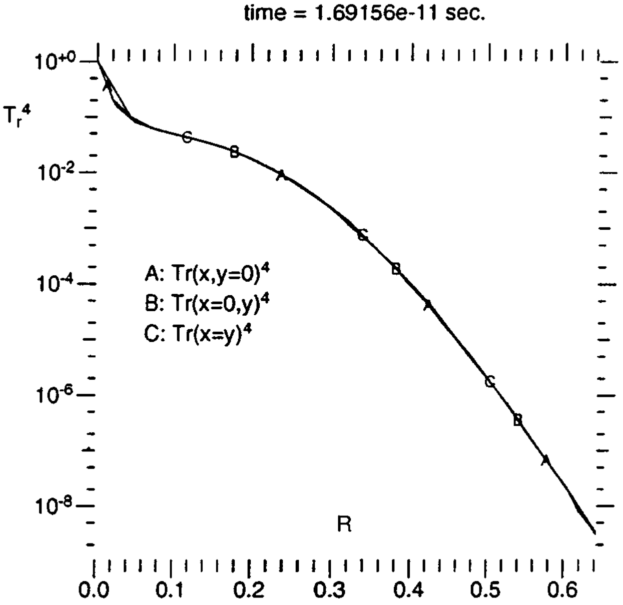

FIG. 7. Flux-limited diffusion; T_r^4 vs. R along (A) $Y = 0$ plane, (B) $X = 0$ plane, and (C) $X = Y$ planes.

3.2.2. Flux-Limiter. In order to show the effectiveness of the limiter, we set $\kappa_P = 0$ and $\ell_R = 1000.0$ and solve Eqs. (14) in the domain $0 \leq X, Y \leq 1$. We define the radiation temperature T_r using the relationship

$$E_r = (4\sigma/c)T_r^4.$$

We initialize with $T_r = 10^{-6}$ everywhere, and at the origin fix $T_r = 1.0$. Symmetry conditions are imposed along $X = 0$ and $Y = 0$. Along $X = 1$ and $Y = 1$, we impose $(c/2)E_r + D_r\partial E_r/\partial n = 0$ which allows radiation to stream out of the problem.

We run the simulation until $t_f \approx 0.5/c = 1.67 \cdot 10^{-11}$ s. At this time, E_r should not extend beyond $R = \sqrt{X^2 + Y^2} = 0.5$. In the absence of flux-limiting, $\min(T_r^4) = 0.99$ over the entire domain, i.e., the cavity fills with radiation. However, when the flux-limiter is on, we obtain the results shown in Fig. 7 which displays T_r^4 along three planes. Although the limiter does not stop all radiation from moving faster than c, at $R = 0.5$ the amount of radiation filling the cavity beyond $R = 0.5$ is only 10^{-3}%.

If in Eq. (26) the number 2 is replaced by another number $a \geq 1$, the effect for small Δt reduces the flux to cE_r/a and the consequence of this change is evident in Fig. 7 from the result at $R = 0.5 \times (a/2)$. For example, if $a = 1$, Fig. 7 shows that $E_r = 8 \times 10^{-3}$ at $R = 0.25$.

The limiter is insensitive to grid distortions. In Fig. 8 we overlay contours of T_r^4 on top of a mesh constructed by giving random displacements to uniformly spaced points. Note how well circular symmetry is maintained.

3.3. *Boundary Flux Accumulation*

In this section we describe the procedure that accumulates fluxes at the problem boundary. Consider the diffusion equation

$$g\partial_t u = -\nabla \cdot \mathbf{F}, \tag{30}$$

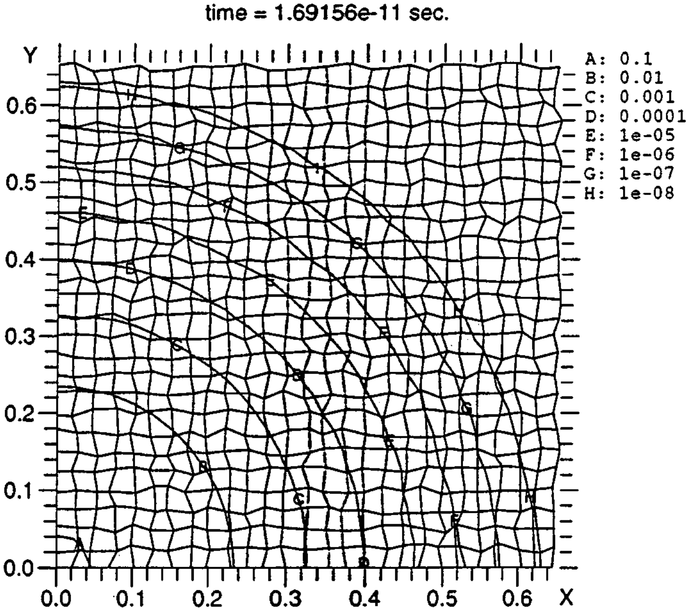

FIG. 8. Flux-limited diffusion. Contours of T_r^4 for levels (A) 0.1, (B) 0.01, . . . (H) 10^{-8}.

where $\mathbf{F} = -D\nabla u$. In our applications, such equations have units of (energy density)/time. In the heat conduction equation, $g = \rho c_\mathrm{v}$ and $u = T$, while for radiation $g = 1$ and $u = E_r$. In the following discussion we assume $g = 1$.

Equation (30) is in conservation form. Integrating over all space and time and defining the energy

$$U(t) = \int_\Omega dV\, u(x, t)$$

yields

$$U(t) = U(0) - \int_0^t d\tau \oint_{\partial\Omega} dA\, \mathbf{F} \cdot \hat{\mathbf{n}}, \tag{31}$$

where $\hat{\mathbf{n}}$ is the outward normal. Boundary conditions for Eq. (30) are either of Dirichlet or mixed type. In the former, on some portion of the boundary $\partial\Omega$, $u = u_d$ where u_d is known. In the latter type, the boundary condition is of the form

$$au - \mathbf{F} \cdot \hat{\mathbf{n}} = b, \tag{32}$$

where $a, b \geq 0$.

In the FE discretization of Eq. (30) a mixed boundary condition poses little difficulty since the boundary integral arises naturally. Equation (32) is implemented by discretizing over the faces that constitute $\partial\Omega$. The discretization reduces to computing

$$\oint_{\partial\Omega} dA(au - b)$$

over each boundary face. Hence, it is easy to determine the amount of energy that flows through $\partial\Omega$.

Calculation of the boundary flux due to Dirichlet conditions is not as straightforward and is done as follows. First, since Dirichlet conditions are imposed on points, it is convenient to define the collection of all mesh points as

$$\mathcal{X} = \mathcal{X}_1 \cup \mathcal{X}_d,$$

where, if x is a mesh point,

$$\mathcal{X}_1 = \{x : u(x) \text{ is unknown}\} \quad \text{and} \quad \mathcal{X}_d = \{x : u(x) = u_d(x)\}.$$

Thus, we express u as a sum of where it is unknown and where it has Dirichlet data,

$$u(x) = \sum_{x_i \in \mathcal{X}_1} \phi_i(x) u_i + \sum_{x_d \in \mathcal{X}_d} \phi_d(x) u_d.$$

For the FE discretization of Eq. (30), the temporal derivative is discretized as $(u - u^0)/\Delta t$, and the equation is multiplied by $\Delta t\, \phi_i$ and integrated over Ω. After lumping the lower order term, this yields

$$\left(\int_\Omega dV\, \phi_i\right)\left(u_i - u_i^0\right) = -\Delta t \int_\Omega dV\, \phi_i \nabla \cdot \mathbf{F}, \tag{33}$$

where ϕ_i is centered on some $x_i \in \mathcal{X}_1$.

Without loss of generality, we assume that if there is a mixed boundary condition, it is homogeneous, i.e., $a = b = 0$ in Eq. (32). Then, after integrating by parts we obtain

$$\int_\Omega dV\, \phi_i \nabla \cdot \mathbf{F} = \sum_{x_j \in \mathcal{X}} \int_\Omega dV\, D \nabla\phi_i \cdot \nabla\phi_j\, u_j, \tag{34}$$

and we stress that $x_i \in \mathcal{X}_1$ and $x_j \in \mathcal{X}$, i.e., we solve equations only on mesh points $x_i \in \mathcal{X}_1$.

If Eq. (34) is substituted into Eq. (33) and the result summed over all $x_i \in \mathcal{X}_1$, we obtain a discretized version of the energy change over a time step. However, the result looks more natural if we add the null quantity

$$\sum_{x_d \in \mathcal{X}_d} \left\{ \int_\Omega dV\, \phi_d \left[\left(u_d - u_d^0\right) + \left(u_d^0 - u_d\right)\right] \right\}.$$

If we now define the discrete analogue of the total energy

$$\tilde{U} \doteq \sum_{x_j \in \mathcal{X}} \int_\Omega dV\, \phi_j u_j,$$

and let $\tilde{U}^0$ represent the energy at the previous time level, we obtain the energy change

$$\tilde{U} - \tilde{U}^0 = \sum_{x_d \in \mathcal{X}_d} \int_\Omega dV\, \phi_d \left(u_d - u_d^0\right) + \mathcal{F}_d, \tag{35}$$

where

$$\mathcal{F}_d = -\Delta t \sum_{x_i \in \mathcal{X}_1} \sum_{x_j \in \mathcal{X}} \int_\Omega dV\, D \nabla\phi_i \cdot \nabla\phi_j u_j \tag{36}$$

is the energy that enters across that portion of Ω_d where we are given Dirichlet data.

The energy change is composed of two terms. The first term on the right side of Eq. (35) represents the temporal change of the Dirichlet data. The second term $\mathcal{F}_d$ vanishes everywhere except on cells which have a point $x_d \in \mathcal{X}_d$. Hence, if we define $\Omega = \Omega_1 \cup \Omega_d$ where

$$\begin{aligned} \Omega_1 &= \{\text{cells : all its vertices } x_i \in \mathcal{X}_1\} \\ \text{and} \quad \Omega_d &= \{\text{cells : with at least one vertex } x_d \in \mathcal{X}_d\}, \end{aligned}$$

then $\mathcal{F}_d$ reduces to integrating only over the cells in Ω_d and is computed after the solution is known since it involves values of u on unknown points. The computation of $\mathcal{F}_d$ requires saving (or recomputing) the contribution to the matrix elements that stemmed from discretizing the diffusion operator over the cells $\in \Omega_d$.

Finally, if the location of Dirichlet data changes from one time level to another, Eq. (35) still holds if the sets $\mathcal{X}_d$ and Ω_d define the points and related cells over the current time cycle.

4. ICF CAPSULE IMPLOSION

To demonstrate the efficiency and robustness of the coupling scheme, we consider a problem of interest in ICF and simulate the implosion of a NIF capsule which consists of a nearly vacuous inner region enclosed by two spherical shells. The capsule dimensions, materials, and initial densities are given in Table VI. The material EOSs are given by the LANL SESAME tables [26]. Since the tables do not have data at low temperatures, we initialize with $T = 0.007$ keV.

The simulation uses the hydrodynamic, heat conduction, and radiation transport packages and is run in the Lagrangian mode. Since the code convects the mass fractions [2], there is some “mixing” of materials across the original Be–D interface (limited to 2–3 cells). Material properties, e.g., κ_P, of cells with pure Be or pure D are calculated by EOS function calls. For the mixed cells, we use the technique described in Section 3.1. In the heat conduction module, the conductivity is given by the Lee & More formulae [21, 23] with modifications suggested by G. Zimmerman [22].

As boundary conditions, for the hydrodynamics, we set $p = 58.22$ GPa on the surface of the capsule which corresponds to the pressure of Be at $\rho = 1.85$ and $T = 0.001$ keV. For the heat conduction package, a symmetry condition is imposed, and for the radiation we use Eq. (32) where $a = c/2$, $u = E_r$, $\mathbf{F}$ is the radiative flux, $b = cE_s/2$, and E_s is set in accordance with a radiation temperature $T_r = 0.16$ keV. The boundary conditions simulate a capsule inside a hohlraum kept at constant T_r.

TABLE VI
NIF Capsule[a]

Dimensions	Material	Density
$r \le r_g = 0.1$	Deuterium	10^{-3}
$r_g \le r \le r_f = 0.11$	Deuterium	0.21
$r_f \le r \le r_a = 0.121$	Beryllium	1.85

[a] Lengths in cm, density in g cm^{-3}.

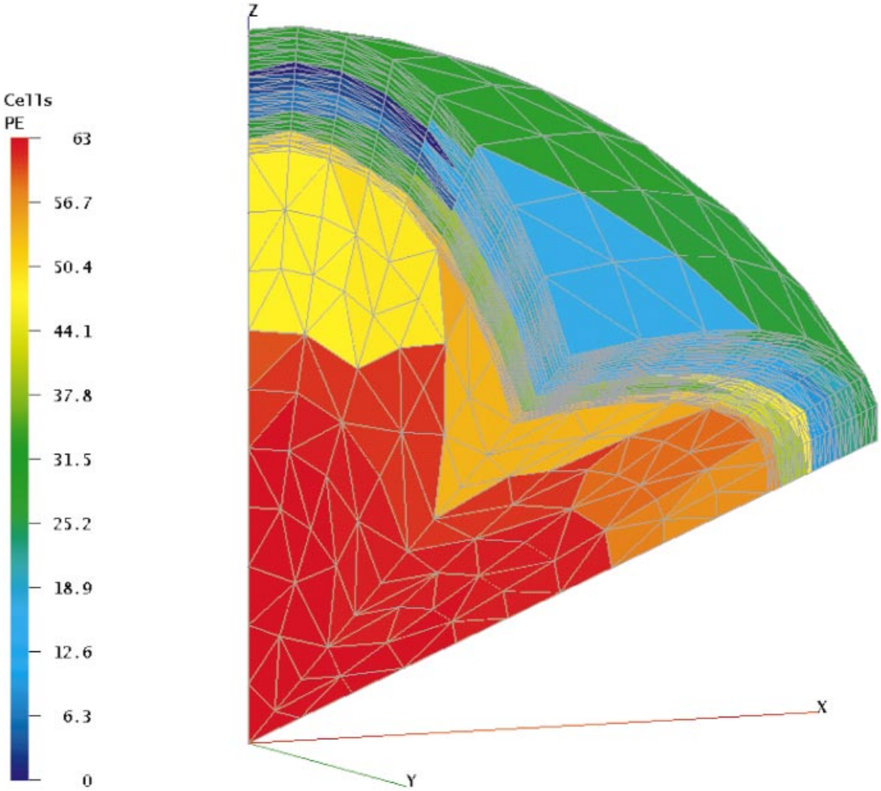

FIG. 9. 3D domain of ICF capsule implosion problem. Shading designates processor numbers. Grid consists of 5,104 tetrahedra, 1,246 points, and 10,915 faces; radial discretization uses 10 cells in the gas, 12 cells for the fuel, and 11 for the ablator.

The computational domain consists of an icosahedral wedge discretized by an unstructured tetrahedral grid generated by the LaGriT code [27] and is decomposed into 64 subdomains using METIS [28]. The initial mesh is displayed in Fig. 9.

The simulation consists of a typical (albeit not well tuned) "indirectly driven" implosion. Energy is deposited on the outer surface of the Be ablator surface which heats up, expands, and creates an imploding shock. The shock traverses first the ablator, then the fuel (where initially $\rho_{\text{Deuterium}} = 0.21$), and later the gas. At both interfaces, $r = r_f$ and $r = r_g$, the shock travels from a high-density region to one of lower density, a scenario for a possible Richtmyer–Meshkov instability. In the ablator, the radiation source is delivered to a thinning, moving spherical surface, a condition ripe for Rayleigh–Taylor instabilities as the tenuous hot outer region pushes on the denser shocked ablator. In Figs. 10, 11, and 12 we present side-on views of ρ, T, and the radiation temperature T_r at $t = 8 \cdot 10^{-9}$ s when the imploding shock has reflected off the origin. Only the central region is displayed.

The figures are characteristic of a capsule implosion. The thin, imploding shell is evident in Fig. 10 which highlights the high-density region. Figure 11 shows that $T = 0.716$ keV near the origin. Outside the central region, out to the ablation front, T is relatively cold. Beyond the ablation front, $T \approx 0.158$ keV due to its coupling to T_r. In Fig. 12 we see the ablation front, outside of which $T_r = 0.158$ keV. Inside the front, T_r is relatively cold, approximately 0.018 to 0.03 keV, while in the central region $T_r \approx 0.075$ keV due to its

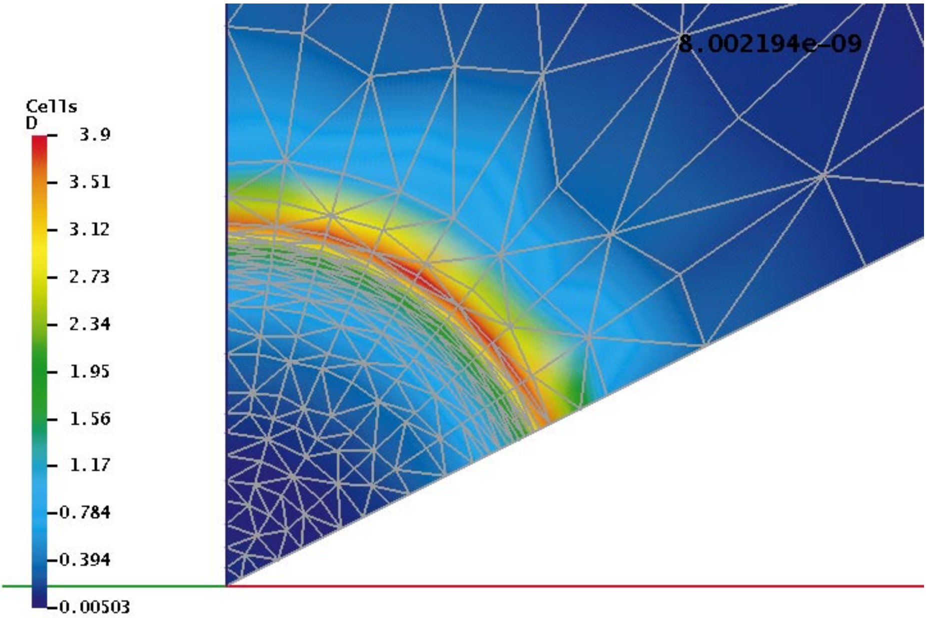

FIG. 10. ICF capsule implosion; side-on view of density; $t = 8 \cdot 10^{-9}$ s.

coupling to T. All three figures clearly display the near spherical symmetry of the implosion. Figure 13 displays lineouts of the results along the Z-axis.

In order to demonstrate that the simulation is qualitatively converged, we make an additional simulation while running the code in "1D" spherical mode, i.e., using only one cell in the azimuthal and polar directions. The 1D run uses slightly finer zoning; Fig. 14 displays

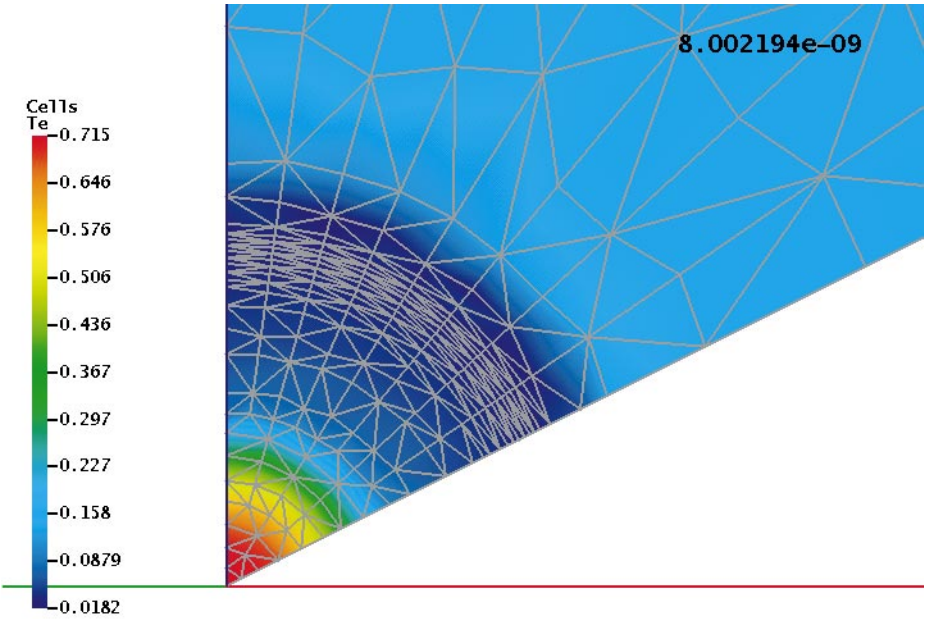

FIG. 11. ICF capsule implosion; side-on view of matter temperature; $t = 8 \cdot 10^{-9}$ s.

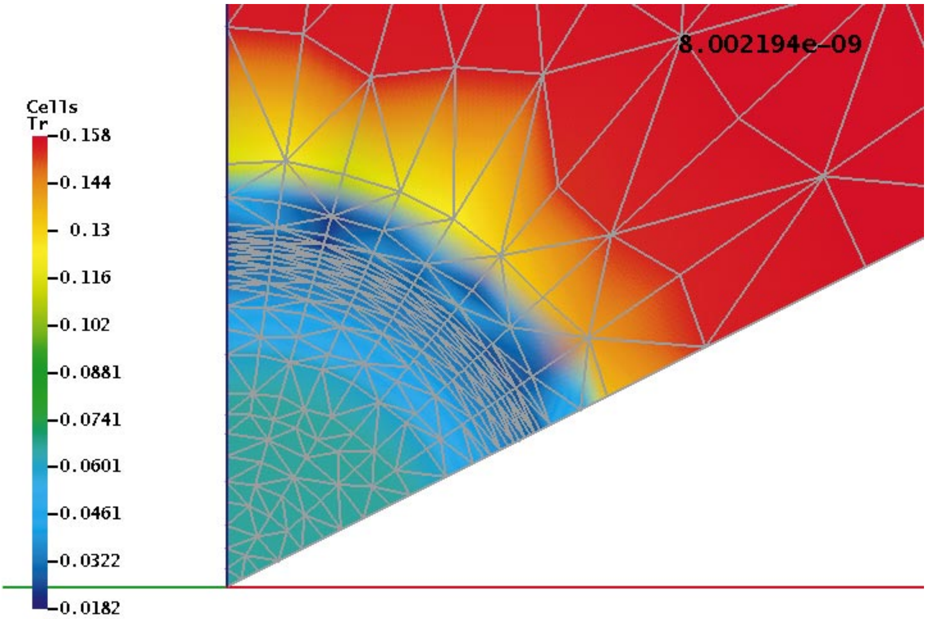

FIG. 12. ICF capsule implosion; side-on view of radiation temperature; $t = 8 \cdot 10^{-9}$ s.

results at $t = 8 \cdot 10^{-9}$ s. Although there are obvious differences between Fig. 14 and the results in Figs. 10–13, the simulations generally agree, especially noting that the meshes are coarse, and that the 3D results are obtained while running in Cartesian coordinates on a tetrahedral grid while the 1D results use spherical coordinates. In Fig. 14, we also see a

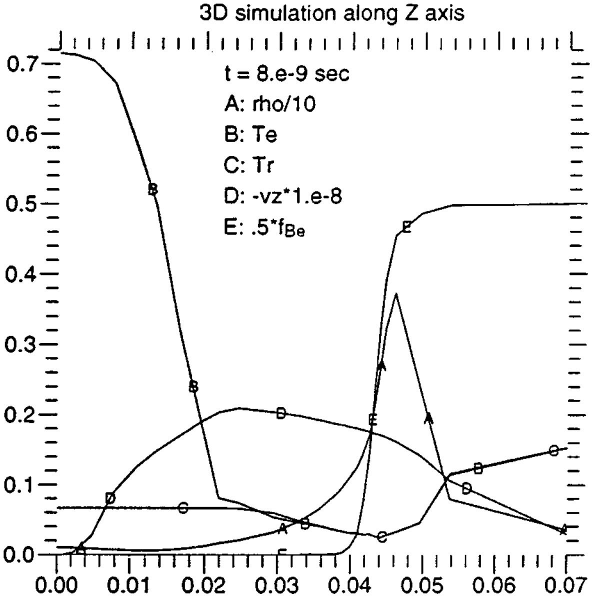

FIG. 13. ICF capsule implosion. Lineout of 3D simulation along the Z-axis. Curve A is $\rho/10$ (g cm^{-3}/10), curves B and C are T and T_r, respectively (keV), curve D is $-\mathrm{vz}/10^8$ (cm s$^{-1}/10^8$), and curve E is the Be mass fraction divided by 2; $t = 8.0 \cdot 10^{-9}$ s.

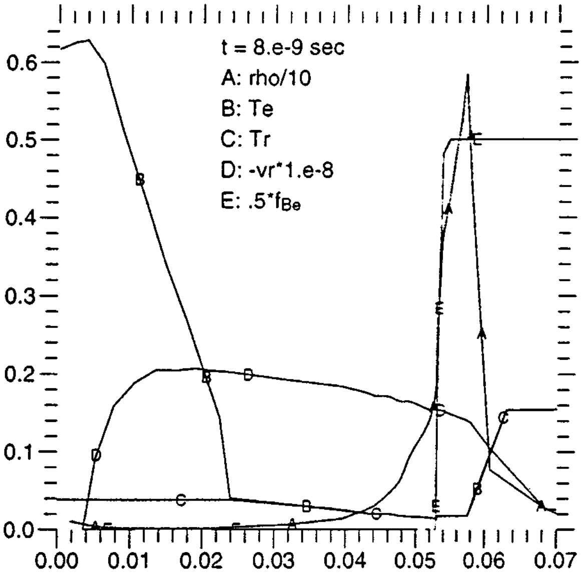

FIG. 14. ICF capsule implosion, 1D run. Curve A is $\rho/10$ (g cm^{-3}/10), curves B and C are T and T_r, respectively (keV), curve D is $-$vr/10^{8} (cm s^{-1}/10^{8}), and curve E is the Be mass fraction divided by 2; $t = 8.0 \cdot 10^{-9}$ s.

thin, imploding shell (curve A), a high central T (curve B), and inside the ablation front at $r \approx 0.06$, a relatively cold T_r (curve C). The large negative velocity depicted in Curve D shows that there is still a great deal of imploding kinetic energy. Finally, curve E is the Be mass fraction, initially a step function centered at $r = 0.11$ cm.

5. CONCLUSION

We have presented an overview of a 3D, unstructured-grid code written to simulate ICF experiments. Special attention has been paid to coupling the seemingly incompatible cell-centered hydrodynamic and point-centered diffusion packages. Mixing the two types of centerings avails us of the best methods for the individual modules. The coupling has proved robust, even on difficult problems such those described in Sections 2 and 4. The 3D implosion simulation maintains the expected symmetry of the solution even though the underlying grid has small scale asymmetries.

APPENDIX: ORDERING OF PHYSICS PACKAGES

In this section we discuss why the time cycle evolves the packages in the order described in Section 2. Our choice is motivated by a desire to obtain the correct answer in the limiting case that the physics equilibrates at the end of the time cycle. However, before discussing this limit, we note that codes such as ours must simulate at least two processes: compressible hydrodynamics and energy transport. The former is described by the (hyperbolic) Euler equations for the conservation of mass, momentum, and energy. For the latter, there are several possibilities. A detailed treatment requires separate ion and electron temperatures and an additional system governing the flow of radiation energy and its coupling to the matter (electrons). Typically, ion and electron energy fluxes are modeled by Fick's law—energy flows down the respective temperature gradient—which leads to diffusion equations. For radiation, a complete description of an intensity dependent on position, time, frequency, and propagation direction is very expensive. Thus, simplifications are made; the most common (and viable for a 3D code) is to assume near isotropy, i.e., ignore directionality. This leads to diffusive transport. Discretizing the frequency spectrum into a number of groups leads to one equation per group, while averaging over the entire spectrum gives rise to the diffusion equation for the radiation energy density E_r.

To continue the simplification, the ion heat conduction equation is either ignored (since its diffusion coefficient is less than the electron's by a factor of $\sqrt{m_i/m_e}$ [19]) or averaged with the electron. This leads to the "2T" model with diffusion equations for T_e and E_r. In some cases, the matter heat conduction is entirely ignored, matter and E_r are assumed to be tightly coupled, i.e., $E_r \approx B = aT^4$, and the energy transport is expressed in terms of a single diffusion equation. The plasma is thus modeled by the Euler equations with heat conduction—the system considered by Reinicke and Meyer-ter-Vehn [11]. Hence, we first motivate how to advance a system consisting of hydrodynamics, heat conduction (diffusion), and an external energy source such as a laser.

The equilibrium limit is obtained if the processes are ordered so as to do the slowest one first. In our applications, since sound speeds are relatively slow, the hydrodynamics package is called first. After the hydrodynamics, which moves material through the mesh, we calculate material properties such as the opacities and the specific heat. In a strictly Lagrangian code, material properties could be calculated first. However, with an Eulerian or ALE hydrodynamic module, material properties are calculated after the matter has moved to its new position. Since laser energy deposition depends on the electron number density n_e, that package follows the calculation of material properties. The laser package cannot be placed at the end of the time cycle since such energy deposition is very localized and enormously raises the temperature in a small region. Thus, processes such as heat conduction and radiation come last in the time cycle since they redistribute the energy source. This procedure implies an additional subtlety. Since the equations are nonlinear, one might propose that each process should be solved either fully nonlinearly or if advanced using "lagged" material properties, these properties should be recomputed after each process. For the laser, this implies recomputing properties such as opacities and specific heats after depositing the laser's energy. This leads to coefficients (used by subsequent modules) that are wildly out of equilibrium. Thus, in a code with only hydrodynamics, a laser, and heat conduction, we advance them in that order. (Properties such as the pressure, since they are needed by the hydrodynamics, are computed at the end of the time cycle.) The laser package comes after the hydrodynamics to avoid anomalous motion due to the localized energy deposition.

We now discuss the ordering of the two diffusion packages: electron heat conduction and (diffusive) radiation transport. Both are flux-limited; the former limits to the thermal speed ($\approx\sqrt{kT/m_e}$), while the latter to the speed of light c. Thus, ordering by the maximum speed of propagation places the radiation last in the time cycle. Another reason for diffusing T before E_r stems from comparing the diffusion coefficients of the set of equations that are advanced after the laser package,

$$\begin{aligned}\rho c_{\mathbf{v}} \partial_t T &= \nabla \cdot D_e \nabla T - \mathcal{K}(B - E_r) + S_e \\ \partial_t E_r &= \nabla \cdot D_r \nabla E_r + \mathcal{K}(B - E_r) + S_r,\end{aligned} \tag{A.1}$$

where $B = aT^4$ is the Planck function, $\mathcal{K} = c\rho\kappa$ is the electron–radiation coupling coefficient, and the S are the explicit sources, e.g., S_e is the energy deposited by the laser.

In most problems, $\mathcal{K}$ is very large. Indeed, the derivation that deletes the radiation's dependence on propagation angle, i.e., that assumes near isotropy, assumes tight coupling to the matter. That is, to a good approximation, $E_r \approx B$. Of course, one approach is to solve the entire system (A.1) simultaneously. Unfortunately, since we require implicit temporal differencing, this leads to linear systems of order $2N$, where N is the number of points. Since the most we wish to tackle is systems of order N, we need to choose which to diffuse last, T or E_r. Heuristically, because of the faster propagation speed, E_r should be last. The following argument affirms that choice.

We assign to last place in the time cycle the most equilibrating (mathematically, the *stiffest*) process, i.e., the one with the largest diffusion coefficient. Before comparing them, we normalize the coefficients. Since we measure temperature in keV, in (A.1), D_e and D_r have units of erg/(cm s keV) and cm^2/s, respectively. The electron diffusion coefficient is [19]

$$D_e = \xi \frac{k(kT)^{5/2}}{m_e^{1/2} Z e^4 \ln\Lambda} = \xi \cdot 1.0 \cdot 10^{20} \frac{T^{5/2}}{Z \ln\Lambda} \left(\frac{\text{erg}}{\text{cm s keV}}\right), \tag{A.2}$$

where $\xi = \mathcal{O}(1)$ and $\ln\Lambda$ is the Coulomb logarithm. The radiation coefficient $D_r = c\ell_R/3$ where ℓ_R is the Rosseland-averaged mfp. The assumption $E_r \approx aT^4$ yields a radiation flux $-D_r'\nabla T$ where

$$D_r' = (4/3)ac\ell_R T^3$$

and $a = 1.37 \cdot 10^{14}$ (erg/cm^3 keV^4). We now include the temperature dependence of ℓ_R. Assuming an opacity given by only free–free transitions [20],

$$\ell_R = 2.6 \cdot 10^{49} \frac{T^{7/2}}{Z^2 n_+ n_e} \text{cm}.$$

Expressing $n_e = Zn_+$ and $n_+ = \rho/Am_p$, where A is the atomic weight and m_p is the proton mass, yields

$$D_r' = 3.9 \cdot 10^{26} \frac{A^2}{\rho^2 Z^3} T^{13/2} \left(\frac{\text{erg}}{\text{cm s keV}}\right). \tag{A.3}$$

Combining (A.2) and (A.3) yields the ratio,

$$\frac{D_r'}{D_e} = 3.9 \cdot 10^6 \left(\frac{A}{Z}\right)^2 \left(\frac{\ln\Lambda}{\xi}\right) \left(\frac{T^4}{\rho^2}\right). \tag{A.4}$$

We now reason that since $\xi = \mathcal{O}(1)$, $A/Z = \mathcal{O}(1)$, and $\ln\Lambda \geq 2$, the factor multiplying (T^4/ρ^2) is of order $8 \cdot 10^6$. Thus, for high temperatures and low densities, radiation diffusion dominates.

REFERENCES

1. A. I. Shestakov, M. K. Prasad, J. L. Milovich, N. A. Gentile, J. F. Painter, and G. Furnish, The Radiation–hydrodynamic ICF3D code, *Comput. Meth. Appl. Mech. Eng.* **187**, 181 (2000).

2. D. S. Kershaw, M. K. Prasad, M. J. Shaw, and J. L. Milovich, 3D unstructured mesh ALE hydrodynamics with the upwind discontinuous finite element method, *Comput. Meth. Appl. Mech. Eng.* **158**, 81 (1998).

3. D. S. Kershaw, Differencing of the diffusion equation in Lagrangian hydrodynamic codes, *J. Comput. Phys.* **39**(2), 375 (1981).

4. G. J. Pert, Physical constraints in numerical calculations of diffusion, *J. Comput. Phys.* **42**, 20 (1981).

5. A. I. Shestakov, J. A. Harte, and D. S. Kershaw, Solution of the diffusion equation by finite elements in Lagrangian hydrodynamic codes, *J. Comput. Phys.* **76**(2), 388 (1988).

6. J. E. Morel, J. E. Dendy, Jr., M. L. Hall, and S. W. White, A cell-centered Lagrangian-mesh diffusion differencing scheme, *J. Comput. Phys.* **103**, 286 (1992).

7. M. Shashkov and S. Steinberg, Solving diffusion equations with rough coefficients in rough grids, *J. Comput. Phys.* **129**, 383 (1996).

8. J. Hyman, M. Shashkov, and S. Steinberg, The numerical solution of diffusion problems in strongly heterogeneous non-isotropic materials, *J. Comput. Phys.* **132**, 130 (1997).

9. J. E. Morel, R. M. Roberts, and M. J. Shashkov, A local support-operators diffusion discretization scheme for quadrilateral r–z meshes, *J. Comput. Phys.* **144**, 17 (1998).

10. W. F. Noh, *Errors for Calculations of Strong Shocks Using an Artificial Viscosity and an Artificial Heat Flux*, UCRL-53669, Lawrence Livermore National Laboratory Report, Livermore, CA, 1985.

11. P. Reinicke and J. Meyer-ter-Vehn, *Phys. Fluids* A **3**(7), 1807 (1991).

12. J. H. Bolstad, personal communication, Lawrence Livermore National Laboratory, 2000.

13. A. I. Shestakov, Time-dependent simulations of point explosions with heat conduction, *Phys. Fluids* **11**(5), 1091 (1999).

14. T. B. Kaiser, Laser ray tracing and power deposition on an unstructured three-dimensional grid, *Phys. Rev. E* **61**, 895 (2000).

15. A. I. Shestakov, J. L. Milovich, and M. K. Prasad, Description of a parallel, 3D, finite element, hydrodynamics–diffusion code, in *Proceedings of the NAFEMS World Congress '99 on Effective Engineering Analysis*, v. 1, *1999*, (NAFEMS, Glascow, UK), p. 273. Available at: www.nafems.org.

16. A. I. Shestakov, J. L. Milovich, and D. S. Kershaw, Parallelization of an unstructured-grid, laser fusion design code, applications on advanced architecture computers, *SIAM News* **32**(3), 6(1999).

17. A. I. Shestakov and J. L. Milovich, *Parallelization Scaling Study of a 3D, Unstructured-Grid. ICF Design Code Using 4 to 1024 Processors*, UCRL-JC-139442, Lawrence Livermore National Laboratory Report, Livermore, CA, 2000.

18. Ya. B. Zel'dovich and Yu. P. Raizer, *Physics of Shock Waves and High-Temperature Hydrodynamic Phenomena* (Academic Press, San Diego, 1966).

19. Ya. B. Zel'dovich and Yu. P. Raizer, *Physics of Shock Waves and High-Temperature Hydrodynamic Phenomena* (Academic Press, San Diego, 1966). Vol. II, p. 519.

20. Ya. B. Zel'dovich and Yu. P. Raizer, *Physics of Shock Waves and High-Temperature Hydrodynamic Phenomena* (Academic Press, San Diego, 1966). Vol. I, p. 260.

21. R. M. More, Atomic Physics of Laser-Produced Plasmas, in *Handbook of Plasma Physics*, Vol. 3: *Physics of Laser Plasma*, edited by Rubenchik and Witkowski (Elsevier, Amsterdam/New York, 1991), p. 63.

22. G. B. Zimmerman, personal communication, Lawrence Livermore National Laboratory, (1998).

23. Y. T. Lee and R. M. More, *Phys. Fluids* **27**(5), 1273 (1984).

24. G. C. Pomraning, *J. Quant. Spectrosc. Radiat. Transfer* **21**, 249 (1979).

25. B. Su and G. L. Olson, *J. Quant. Spectrosc. Radiat. Transfer* **56**(3), 337 (1996).

26. S. P. Lyon and J. D. Johnson, Eds. *SESAME: The Los Alamos National Laboratory Equation of State Database*. LA-UR-92-3407, Los Alamos National Laboratory Report (1992). Also: T-1 Handbook of Material Properties Data Bases, K. S. Holian, Ed., LA-10160-MS, (1984).

27. `www.t12.lanl.gov/ ~ lagrit`

28. G. Karypis and V. Kumar, A fast and high-quality multilevel scheme for partitioning irregular graphs, *SIAM J. Sci. Comput.* **20**(1), 359 (1998). For METIS program, see `http://www-users.cs.umn.edu/~karypis/metis/metis/main.html`.